J Mater Sci (2008) 43:4550–4560
DOI 10.1007/s10853-008-2639-5

# Modification of alumina scale formation on FeCrAlY alloys by minor additions of group IVa elements

**D. Naumenko · V. Kochubey · L. Niewolak · A. Dymiati · J. Mayer · L. Singheiser · W. J. Quadakkers**

Received: 30 November 2007 / Accepted: 8 April 2008 / Published online: 23 April 2008

**Abstract** The effect of Ti, Zr and Hf minor additions on the alumina scale formation on a high-purity, FeCrAlY model alloy has been studied. Thermogravimetry at 1,200–1,300 °C in Ar–20%$O_2$ and two-stage oxidation using $^{18}O$-tracer were combined with characterisation by electron microscopy and sputtered neutral mass spectroscopy. After oxidation, the incorporation of Hf and Zr into the scale was far more substantial than that of Ti. This is explained by the higher thermodynamic stability of the Zr- and Hf-based oxides because the incorporation occurred to a large extent via an internal oxidation process. The scale growth kinetics is accelerated by incorporation of zirconia precipitates that provide short-circuit paths for oxygen diffusion, reduce the scale grain size and cause formation of porosity. In contrast, the incorporation of Hf-containing oxides has no such accelerative effect on the scale growth kinetics.

## Introduction

FeCrAl alloys are materials used in many high-temperature applications where a high oxidation resistance is required. The alloys are commonly used as construction materials for heating elements, hot zone furnace furniture and more recently in car catalysts and industrial gas heaters. The oxidation resistance is provided by formation of an alumina surface scale, which protects the alloy from rapid environmental degradation. The protective properties of the alumina scale, in particular scale adherence during cyclic oxidation, are improved by the minor additions (less than 1 mass%) of reactive elements (RE), such as Y, La, Ce, Zr, Hf either in metallic form or as oxide dispersions (ODS) [1, 2]. This positive RE effect is attributed to gettering alloy sulphur impurity [3, 4], thus preventing deleterious sulphur segregation to the alumina/alloy interface and to the suppression of outward cationic transport through the alumina scale [5, 6], thus reducing vacancy injection into the oxide/metal interface. Recent microstructural studies [7] indicate that the extent of the cationic transport suppression differs between different REs and depends on their exact contents and combinations. The minor alloy chemistry has been recognised as a crucial factor, which significantly affects the oxidation limited lifetime of the FeCrAl materials, i.e. the time to critical Al depletion for the scale formation followed by the catastrophic breakaway oxidation. Large lifetime differences were reported for alloys of virtually the same major composition, however, with variations of RE and/or impurity contents [8, 9].

Commercial FeCrAl alloys frequently contain several reactive elements [10, 11]. Most of the advanced FeCrAl materials are alloyed with group IIIa elements, Y (less commonly La or Ce) along with group IVa elements (Ti, Zr, Hf). While the group III elements are added to improve the oxidation resistance as discussed above, the primary reason for adding group IVa elements is to facilitate the manufacturing of wrought alloy products, such as ultra thin foils for car catalyst substrates. Ti, Zr and Hf have been found to decrease the DBTT temperature and to prevent the formation of Cr carbides at the alloy grain boundaries, which lead to embrittlement problems during hot rolling

D. Naumenko (✉) · V. Kochubey · L. Niewolak · L. Singheiser · W. J. Quadakkers
Forschungszentrum Jülich GmbH, IEF-2, 52425 Jülich, Germany
e-mail: d.naumenko@fz-juelich.de

A. Dymiati · J. Mayer
Gemeinschaftslabor für Elektronenmikroskopie, RWTH-Aachen, 52074 Aachen, Germany

[12]. The carbon gettering by group IVa additions is also essential from the viewpoint of long-term stability of the alumina scale as pointed out in recent studies on model alloys [13]. It was found that in a model FeCrAlY alloy with a typical carbon impurity level for commercial materials (≈500 mass ppm), formation of brittle chromium carbides at the oxide/metal interface occurs, which promotes alumina scale spallation and premature breakaway failure during cyclic oxidation.

Until now, only limited literature data had been available on the mechanisms behind the effects of IVa element additions on the oxidation behaviour of group IIIa-doped FeCrAl alloys. Similar to the additions of group IIIa elements, RE additions of the group IVa elements have been observed as segregants and/or oxide precipitates at the grain boundaries of the alumina scale as well as at the alumina/alloy interface [6, 11]. In spite of the fact that many commercial alloys contain combined IIIa + IVa RE-additions, these materials are often susceptible to significant batch-to-batch variations in the RE and impurity contents [9]. This makes it rather difficult to attribute a specific observed effect on the oxidation properties to a particular element. To overcome this problem in the present work a number of high-purity Y-containing model FeCrAl alloys with Ti, Zr and Hf additions were procured. Short-term isothermal oxidation tests were performed at 1,200 and 1,300 °C in a thermobalance and in selected cases using oxygen isotopes as oxidising medium. All exposures were followed by detailed characterisation of the formed oxide scales with respect to the microstructures and chemical compositions.

## Experimental

The nominal base composition (mass%) of the studied model alloys was Fe–20Cr–5Al–0.05Y (Alloy Y). To this base composition 0.02%Ti (Alloy Y + Ti), 0.03%Zr (Alloy Y + Zr) and 0.03%Hf (Alloy Y + Hf), respectively, were alloyed. The alloys were melted in a cold crucible under Ar. Sheets of 1 mm thickness produced from the ingots by hot rolling were annealed at 1,000 °C in Ar for 1 h and then water-quenched. The chemical analyses data measured on the wrought sheets are summarised in Table 1.

**Table 1** Chemical compositions[a] of the studied alloys (mass%)

| Alloy | Y | Y + Ti | Y + Zr | Y + Hf |
|---|---|---|---|---|
| Fe | Base | Base | Base | Base |
| Cr | 19.90 | 19.70 | 19.70 | 19.40 |
| Al | 5.00 | 4.91 | 4.86 | 5.00 |
| Y | 0.051 | 0.048 | 0.049 | 0.045 |
| Ti | 0.0015 | 0.022 | 0.0012 | 0.001 |
| Hf | <0.005 | <0.005 | <0.005 | 0.031 |
| Zr | <0.001 | <0.001 | 0.029 | <0.001 |
| Si | 0.002 | 0.001 | 0.0018 | 0.0015 |
| P | 0.0086 | 0.0078 | 0.0078 | 0.0097 |
| C | 0.0092 | 0.0090 | 0.0090 | 0.0115 |
| S | <0.001 | <0.001 | <0.001 | 0.0005 |
| O | <0.001 | <0.001 | <0.001 | 0.0004 |
| N | <0.001 | <0.001 | <0.001 | 0.0006 |

[a] Analysed by inductive coupled plasma mass spectrometry, ICP-MS; except C, S, O (infrared absorption spectroscopy) and N (thermal conductivity analysis)

Specimens of 20 × 10 × 1 mm in size were ground to 1,200 grit surface finish and ultrasonically degreased in ethanol prior to the oxidation exposures. Thermogravimetric (TG) analyses were performed up to 100 h in Ar–20%$O_2$ at 1,200–1,300 °C in a SETARAM® thermobalance. The oxidised specimens were subsequently examined by scanning electron microscopy (SEM), coupled with energy-dispersive X-ray analysis (EDX) and X-ray diffraction analysis (XRD). From selected specimens cross-sections of the oxide scales were prepared using the focused ion beam (FIB) technique and analysed using transmission electron microscopy (TEM). The TEM images were acquired in the scanning transmission electron microscopy (STEM) mode using a high angle annular dark-field (HAADF) detector. For determination of the scale growth mechanisms, two-stage oxidation experiments in oxygen isotopes were performed at 1,200 °C. The specimens were exposed for 4 h in Ar–20%$O_2$ (normal oxygen), then the gas was switched in situ to $^{18}O$ enriched Ar–20%$O_2$ for 16 h. For the latter oxidation stage the $^{18}O$-enrichment was 20% of the total oxygen content. After this two-stage oxidation the specimens were depth-profiled by plasma-induced sputtered neutral mass spectrometry (plasma-SNMS). From the measured elemental intensity profiles, atomic concentration profiles were calculated using the procedure described elsewhere [5]. The oxygen isotope concentrations were calculated using the $^{18}O$-enrichment factor, which would prevail, if the $^{18}O$ content during the second stage would have been 100%.

## Results

Figures 1–4 show the SNMS depth profiles of the alloy specimens after 20 h two-stage isothermal oxidation at 1,200 °C in Ar–20%$O_2$ with oxygen tracers. For all four materials $^{18}O$-isotope profiles exhibit an enrichment at the very scale/gas interface, whereas in the middle of the scale its concentration drops below 10 at.%. The major part of $^{18}O$ is enriched at the scale/metal interface. Therefore, the SNMS profiles indicate [14, 15] that for all studied alloys

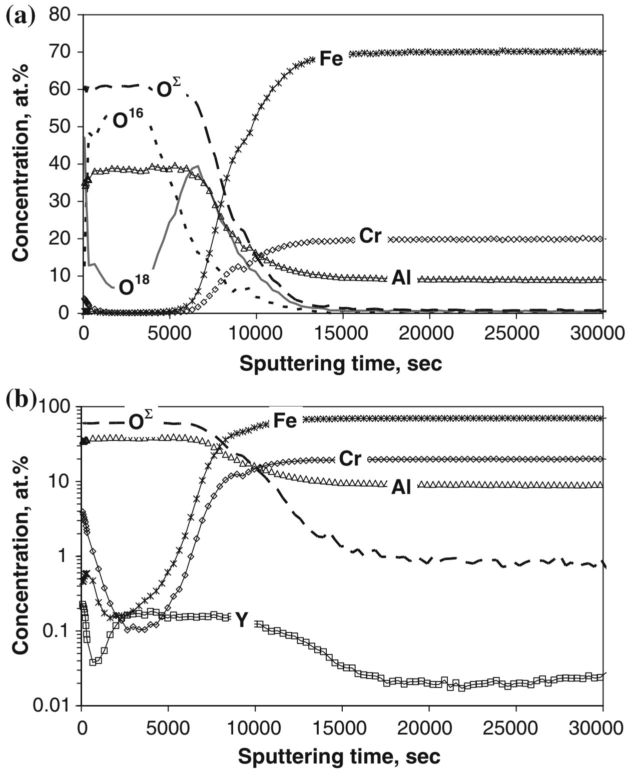

**Fig. 1** SNMS-depth profiles of Alloy Y after two-stage oxidation at 1,200 °C in Ar–20%$O_2$. 1st stage: 4 h in $^{16}O_2$; 2nd stage 16h in $^{18}O_2$-enriched gas: (**a**) linear scale of concentration (**b**) logarithmic scale of concentration showing minor alloying additions

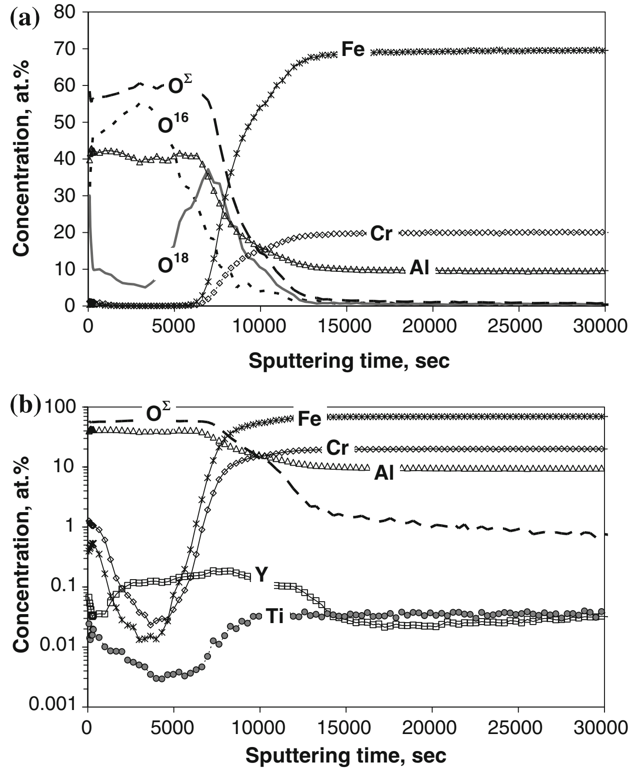

**Fig. 2** SNMS-depth profiles of Alloy Y + Ti after two-stage oxidation at 1,200 °C in Ar–20%$O_2$. 1st stage: 4 h in $^{16}O_2$; 2nd stage 16h in $^{18}O_2$-enriched gas: (**a**) linear scale of concentration (**b**) logarithmic scale of concentration showing minor alloying additions

the predominant oxide growth mechanism is short-circuit oxygen diffusion, apparently via oxide grain boundaries similar to the literature observations for FeCrAl ODS alloys [5]. The reason for the minor $^{18}$O-peak at the gas/oxide interface observed on all studied materials is probably isotope exchange, an effect more pronounced in the outer part of the scale with a high GB density as proposed in [5] or a minor outward RE transport through the scale [6].

In Alloys Y and Y + Ti the measured Y profiles exhibit two characteristic kinks: a steep one near the gas/oxide interface and a flatter one at the oxide/metal interface extending into the metal (Figs. 1b and 2b, respectively). In contrast, in Alloys Y + Zr (Fig. 3b) and Y + Hf (Fig. 4b) hardly any Y enrichment in the oxide scale can be observed, whereas substantial enrichment of Zr and Hf, respectively, prevails. In Alloy Y + Ti the Y profile is similar to that in Alloy Y. With respect to Ti, notable enrichment can only be found at the scale/gas interface, while no Ti incorporation into the inner part of the scale can be observed (Fig. 2b).

Figure 5a shows thermogravimetric data of the studied materials during isothermal oxidation at 1,200 °C in Ar–20%$O_2$. It can be seen that at 1,200 °C the Zr-containing alloy exhibits substantially higher mass changes than the other materials. Figure 5b shows the instantaneous "apparent" parabolic constant, $K'_p(t)$ calculated from the mass change data in Fig. 5a according to the procedure described in Ref. [16], i.e. $K'_p(t) = (\mathrm{d}\Delta m/\mathrm{d}t^{1/2})^2$. This method was used to compare the instantaneous oxidation rates of the studied materials and to determine whether at longer times the kinetics start to approach a parabolic behaviour. It can be seen from Fig. 5b that for Alloys Y, Y + Ti and Y + Hf the $K'_p(t)$ values decrease with increasing exposure time. Due to the fact that the protective alumina scale is established very fast on this material, the decrease in $K'_p(t)$ indicates sub-parabolic scale growth reported previously for Y-containing FeCrAl-alloys by several authors [17, 18]. The $K'_p(t)$ curves for alloy Y + Zr exhibit, however, a different behaviour: after an initial decrease $K'_p(t)$ remains virtually constant at a value, which is a factor of 5 higher than that of the other alloys.

Contrary to the results at 1,200 °C, the isothermal mass changes measured at 1,300 °C of Alloys Y and Y + Zr are comparable, and they are somewhat higher than those of Alloys Y + Ti and Y + Hf (Fig. 6a). At 1,300 °C a monotonic decrease in the $K'_p(t)$ values with time is observed for Alloys Y, Y + Ti and Y+Hf (Fig. 6b),

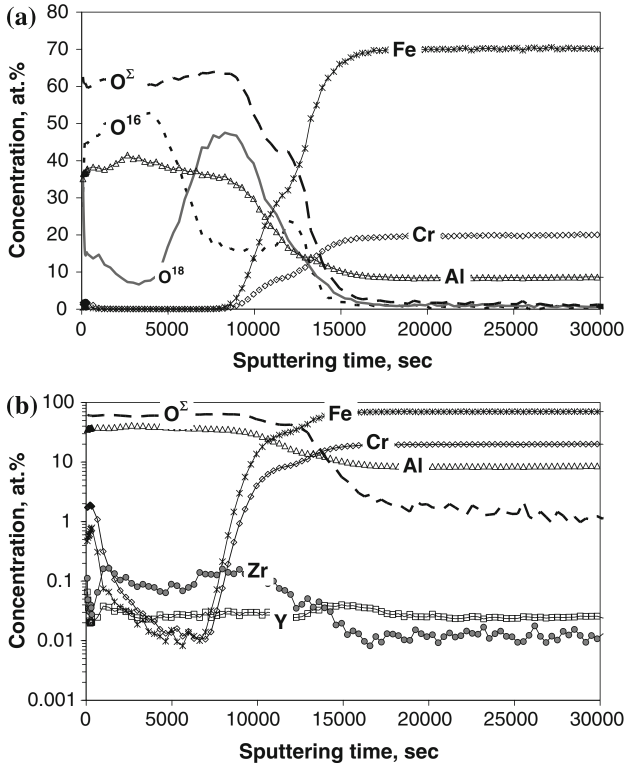

**Fig. 3** SNMS-depth profiles of Alloy Y + Zr after two-stage oxidation at 1,200 °C in Ar–20%$O_2$. 1st stage: 4 h in $^{16}O_2$; 2nd stage 16h in $^{18}O_2$-enriched gas: (**a**) linear scale of concentration (**b**) logarithmic scale of concentration showing minor alloying additions

suggesting sub-parabolic oxidation kinetics. It should be noted that at the end of the tests the absolute $K'_p(t)$ values for the latter two alloys were by a factor of two smaller than those for Alloy Y. For Alloy Y + Zr the $K'_p(t)$ curve deviates initially from the sub-parabolic behaviour showing a "kink" with a maximum at around 30 h of exposure time (Fig. 6b). After longer times the common tendency of $K'_p(t)$ to decrease with time also occurs for Alloy Y + Zr.

The SEM cross-sections in Fig. 7 and XRD patterns in Fig. 8 of the oxide scales formed on the specimens after the TG-tests at 1,200 °C are presented. The alumina scales formed on Alloys Y and Y + Ti (Fig. 7a and b) are uniform in thickness with some Y/Al-mixed oxide inclusions and pegs. The XRD data in Fig. 8 indicate that these mixed oxides are mainly garnets ($Y_3Al_5O_{12}$); however, a smaller fraction of perovskites ($YAlO_3$) was also found. On Alloy Y + Hf the alumina scale has a similar morphology as on Alloys Y and Y + Ti, however, the light oxide precipitates are present within the scale (Fig. 7d), which could be identified by XRD as hafnia ($HfO_2$) and Y/Hf-mixed oxide ($Y_2Hf_2O_7$) (Fig. 8). Alloy Y + Zr shows a different type of oxide morphology (Fig. 7c): a convoluted scale/metal interface indicative of a locally

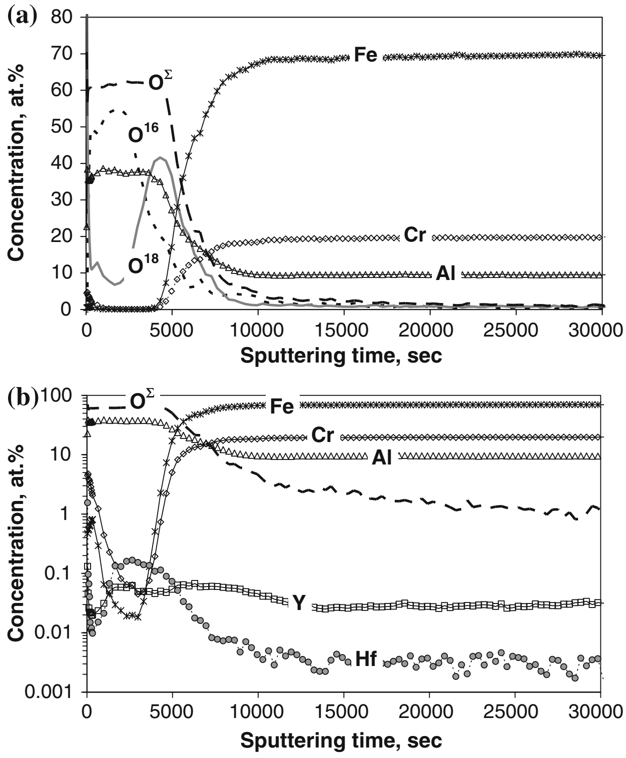

**Fig. 4** SNMS-depth profiles of Alloy Y + Hf after two-stage oxidation at 1,200 °C in Ar–20%$O_2$. 1st stage: 4 h in $^{16}O_2$; 2nd stage 16h in $^{18}O_2$-enriched gas: (**a**) linear scale of concentration (**b**) logarithmic scale of concentration showing minor alloying additions

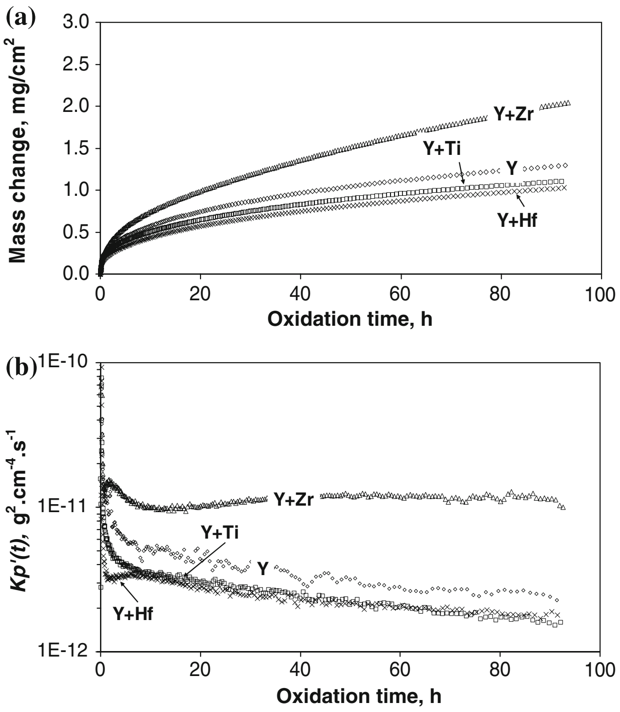

**Fig. 5** (**a**) Mass change data during isothermal oxidation of studied alloys at 1,200 °C in Ar–20%$O_2$ and (**b**) apparent instantaneous parabolic oxidation rate $K'_p(t)$ derived from the mass change data in (a)

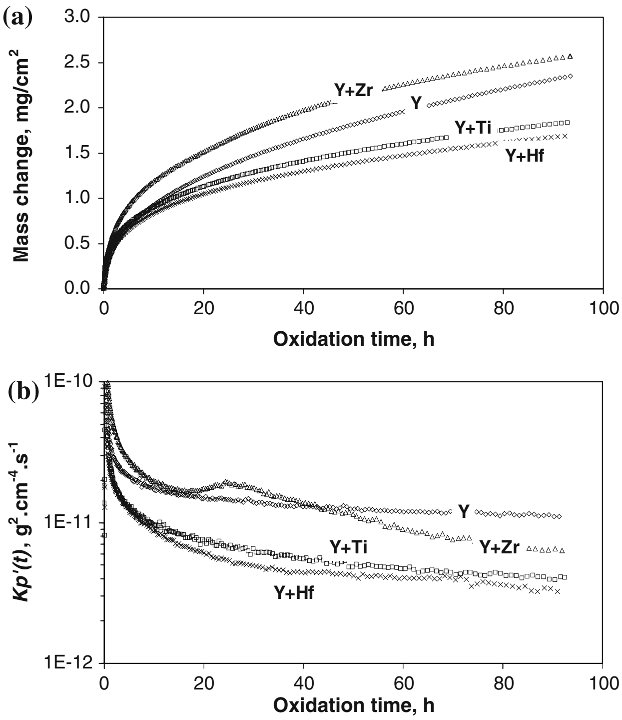

**Fig. 6** (**a**) Mass change data during isothermal oxidation of studied alloys at 1,300 °C in Ar–20%$O_2$ and (**b**) apparent instantaneous parabolic oxidation rate $K'_p(t)$ derived from the mass change data in (a)

enhanced inward scale growth and a number of elongated light oxide particles aligned parallel to the oxide growth direction are present, which were identified as tetragonal zirconia (Fig. 8).

The oxide scale microstructures on the studied alloys after oxidation at 1,200 °C were analysed by TEM (Fig. 9). It is clear that the scales on Alloys Y, Y + Ti and Y + Hf exhibit a columnar grain morphology. In contrast, the scale on Alloy Y + Zr is obviously thicker and the alumina microstructure in the inner part of the scale deviates from the columnar morphology found for the other alloys.

After oxidation for 100 h in Ar–20%$O_2$ at 1,300 °C Alloys Y and Y + Ti show an alumina scale morphology and composition very similar compared to that after oxidation at 1,200 °C (compare Figs. 10 and 7). In contrast, in Alloy Y + Hf the amount of Hf-rich inclusions within the scale and in the sub-scale regions is much larger after oxidation at 1,300 °C than at 1,200 °C. In Alloy Y + Zr the morphology of the zirconia inclusions as well as their distribution within the scale changed substantially upon increasing the temperature from 1,200 to 1,300 °C (compare Figs. 7 and 10). After oxidation at 1,300 °C the zirconia inclusions are larger in size and more equiaxed in morphology than at 1,200 °C and they are present only in the outer part of the scale.

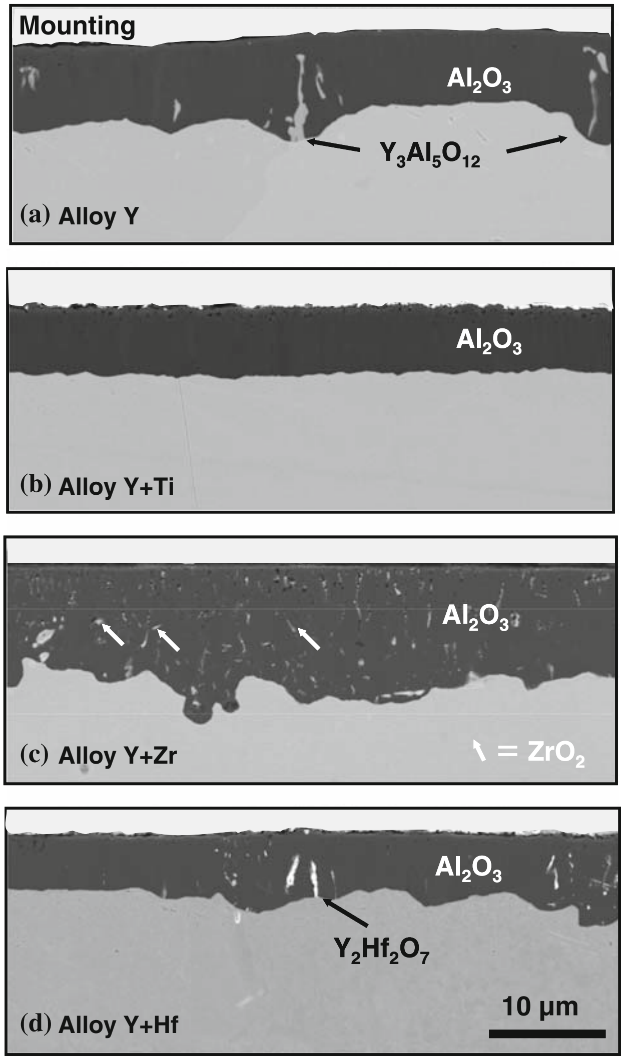

**Fig. 7** SEM cross-sections of the specimens after isothermal oxidation for 96 h at 1,200 °C in Ar–20%$O_2$ for: (**a**) Alloy Y, (**b**) Alloy Y + Ti, (**c**) Alloy Y + Zr, (**d**) Alloy Y + Hf

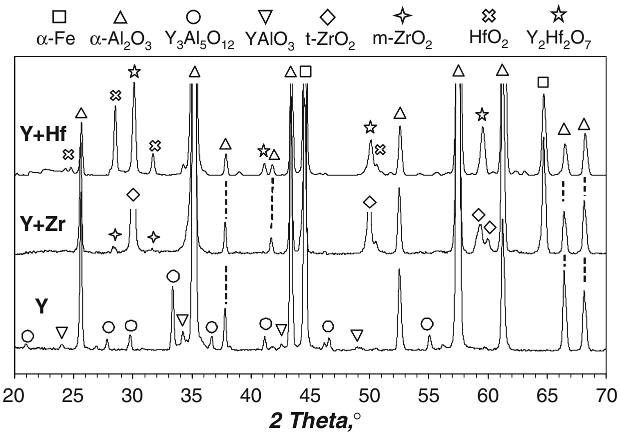

**Fig. 8** XRD Patterns after 100 h oxidation at 1,200 °C in Ar–20%$O_2$ for Alloys Y, Y + Zr and Y + Hf

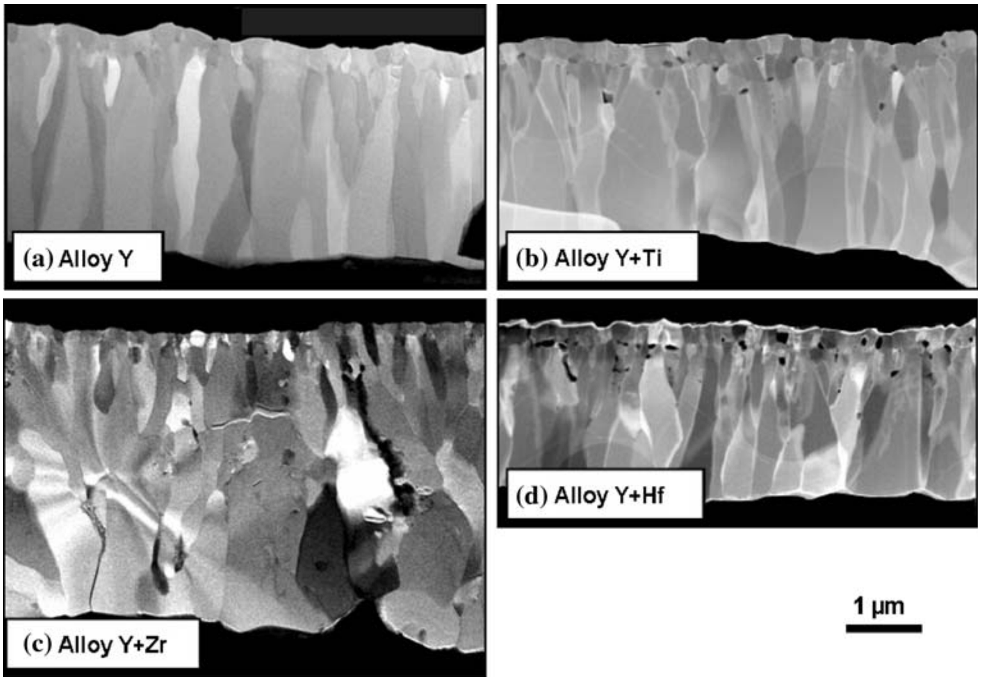

**Fig. 9** STEM-HAADF dark-field images of FIB scale cross-sections after isothermal oxidation for 20 h at 1,200 °C in Ar–20%$O_2$

## Discussion

### RE incorporation into the scale in Alloys Y and Y + Ti

SNMS depth profiles of the samples after two-stage oxidation using $^{16}O$ and $^{18}O$ isotopes indicate that for Alloys Y and Y + Ti the predominant scale growth mechanism is inward short-circuit (grain boundary) diffusion of oxygen. Similar observations were made in earlier studies for other RE-doped FeCrAl materials such as ODS alloys [5]. The shape of the Y profiles in the alumina scales on Alloys Y and Y + Ti can be explained in terms of yttrium reaction with oxygen at different stages of the oxidation process. The Y enrichment at the very oxide surface likely originates from the initial stages of high-temperature exposure due to preferential Y oxidation in accordance with the high thermodynamic stability of Y-containing oxides. Because of preferential, rapid oxidation in the initial stages the Y is depleted in the near-surface regions and its concentration below the surface-enrichment zone drops. At this stage an alumina-based scale develops and yttrium is oxidised internally as indicated by the Y “kink” in the SNMS profile, which extends into the alloy beneath the oxide/metal interface. SEM/EDX data indicate that Y in the oxide scale and in the sub-scale zone is mainly present as Y-Al-Garnet (YAG) precipitates predominantly at the alloy grain boundaries. Comparison of the SEM images with SNMS profiles leads to the conclusion that Y is mainly incorporated into the inwardly growing alumina scale as YAG particles.

Contrary to Y, only minor Ti incorporation into the alumina scale and no internal oxidation of Ti could be observed by SNMS. This observation is in agreement with the thermodynamic stability data, which reveal that at unit metal activities Ti oxide is slightly less stable than alumina. As a consequence, at sufficiently high Al activities, Ti is not expected to be oxidised internally underneath the alumina scale.

The sub-parabolic oxidation rate measured in the TG experiments for Alloys Y and Y + Ti at 1,200 and 1,300 °C is apparently related to the columnar microstructure and growth mechanism (grain boundary oxygen diffusion) of the alumina scale. The latter features are typical for alumina scales on Y or $Y_2O_3$ doped FeCrAl alloys and the correlation between the scale growth mechanism, kinetics and microstructure was illustrated previously [17, 18]. Recently a more accurate description of the grain size has been used to predict cubic scale growth rate at longer oxidation times [19]. A higher oxidation rate of Alloy Y than that of Alloy Y + Ti might be related to the fact that larger amounts of YAG precipitates prevailed in the scale on the former material. Therefore, in the former case a larger density of short-circuit paths for oxygen diffusion could be expected. The exact reason for the effect of Ti on Y distribution in the scale is presently not known and is a subject of an ongoing research.

### RE incorporation into the alumina scales on Alloys Y + Zr and Y + Hf

The alumina scales on Alloys Y + Zr and Y + Hf grow by a similar mechanism as those on the two other alloys, i.e. short-circuit diffusion of oxygen. However, an interesting

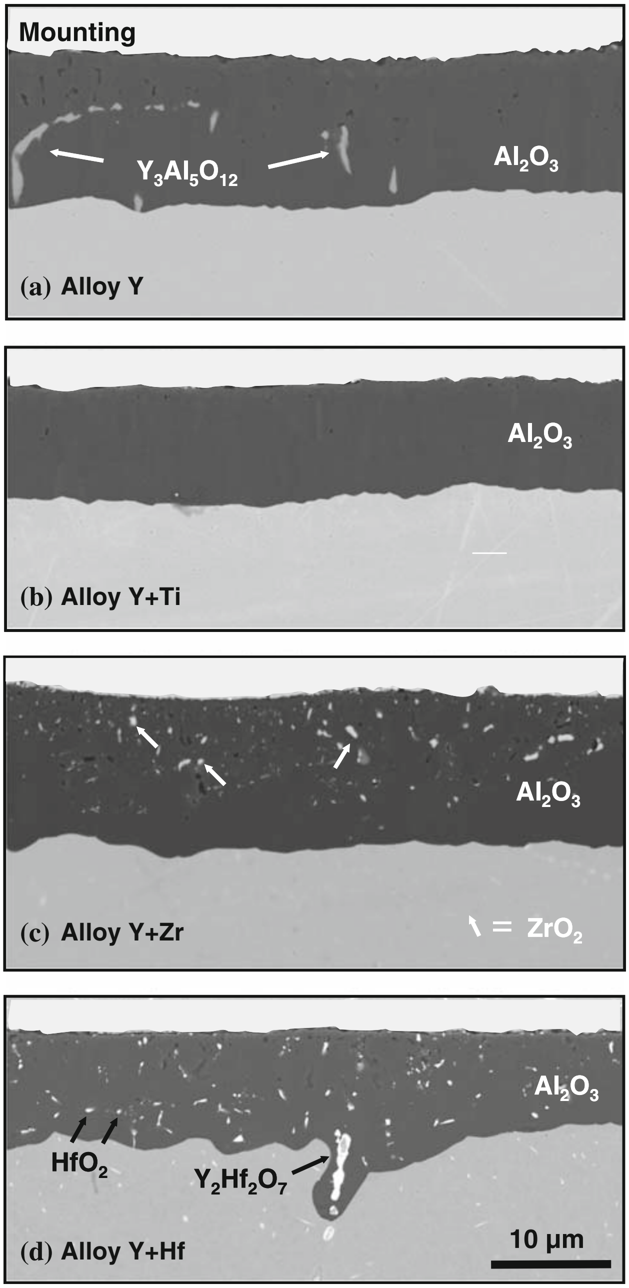

**Fig. 10** SEM cross-sections of the specimens after isothermal oxidation for 96 h at 1,300 °C in Ar–20%$O_2$ for: (**a**) Alloy Y, (**b**) Alloy Y + Ti, (**c**) Alloy Y + Zr, (**d**) Alloy Y + Hf

feature of the SNMS-depth profile on both alloys is that Y incorporation was suppressed and substantial Zr (Hf respectively) incorporation into the oxide scale occurred. This is in agreement with the SEM/EDX studies of Alloy Y + Zr (Y + Hf), whereby no YAG precipitates were found in the alumina scales and sub-scale regions. It is noteworthy that the shapes of the SNMS-depth profiles for Zr and Hf in Alloys Y + Zr and Y + Hf, respectively, are very similar to those for Y in Alloys Y and Y + Ti. This indicates that the mechanism of Zr (Hf) incorporation into the alumina scale is similar to that of Y, i.e. preferential oxidation at the alloy surface in the early oxidation stages followed by internal oxidation with subsequent incorporation of the internal oxides into the inwardly growing alumina scale. The latter mechanism might also explain the minor "kink" in the $^{16}O$-profile at the scale/metal interface on Alloy Y + Zr, which is probably due to strong internal oxidation of Zr in the earlier stages of oxidation.

The suppression of Y incorporation into the scale on the Y + Zr and Y + Hf co-doped alloys can be explained in terms of a higher Zr and Hf mobility in the alloy compared to that of Y. This is indicated by binary alloy phase diagrams, which claim a significantly higher Zr and Hf solubility in high-temperature BCC-Fe ($\delta$-ferrite) compared to that of Y [20–22]. As a consequence of fast Zr (Hf) transport, mainly zirconia (hafnia respectively) internal precipitates are formed in the sub-scale alloy regions. By the oxide precipitation, Zr and Hf getter the oxygen dissolved into the alloy from the oxide/alloy interface and substantially reduce internal oxidation of Y. This idea is supported by detailed analysis of the SNMS profiles. They indicate that the Y incorporation is suppressed to a larger extent in the Zr-containing alloy, which forms a more extensive internal oxide precipitation than in the Hf-containing alloy (Figs. 1–4). The reason for the less pronounced internal oxidation of Hf might be, e.g. the lower Hf content (in at.%) and/or slower Hf mobility in the alloy matrix, compared to those of Zr.

### Effect of Zr on the alumina scale microstructure and growth rate

The extensive incorporation of the zirconia precipitates into the alumina scale results in an enhanced oxidation rate of Alloy Y + Zr compared to that of the other studied materials at 1,200 °C (Fig. 5). First, the zirconia inclusions incorporated into the alumina scale are themselves short-circuit diffusion paths due to the fast oxygen ion transport in zirconia [23]. Second, it is apparent from the SEM images in Fig. 7 that the scale on Alloy Y + Zr exhibits significant porosity, which provides additional short-circuit paths for inward oxygen transport via molecular gas diffusion. The exact mechanism for the formation of porosity requires further investigations. Pint [24] proposed that the pores observed within the scale can originally form at the scale–metal interface between the oxide grain boundaries. Incorporation of the interfacial pores into the scale then occurs [24] by joining the oxide protrusions growing at the nearest grain boundaries. Based on the above results it is unlikely that this mechanism can be operative in the materials studied in the present work. As found in tracer studies, the scale on Alloy Y + Zr grows almost exclusively inwardly. The pores are, therefore, unlikely to form at the scale-metal interface by vacancy condensation. This is in agreement with the SEM and TEM studies, which do not indicate porosity formation at the scale/metal interface. The porosity is mainly observed in the outer part of the scale on Alloy Y + Zr and associated with the zirconia precipitates. Hence, the mechanism for porosity formation might be related to the phase transformations of the zirconia particles caused, e.g. by increase in the oxygen partial pressure [25] in the outer scale regions. Finally, the incorporation of the zirconia particles results in perturbation of the "ideal", columnar grain structure typical [6, 17, 18] for scales formed on FeCrAlY alloys. This is indicated by the TEM image in Fig. 9c, where formation of new grains can be observed in the inner part of the scale on Alloy Y + Zr. Consequently the grain boundary density is higher in the scale on this material compared to the other materials studied. This effect of Zr on the scale microstructure at 1,200 °C is even more apparent at longer exposure times [26], whereby the actual mechanism could be, e.g. grain boundary pinning of the alumina grains by zirconia precipitates, thus preventing grain growth and/or provide nucleation sites for new alumina grains at the scale–metal interface. The higher grain boundary density may be a factor, which in addition to the presence of zirconia inclusions and porosity is responsible for the rapid scale growth on Alloy Y + Zr at 1,200 °C.

Different to the 1,200 °C results the mass change of Alloy Y + Zr after 100 h at 1,300 °C is comparable to that of Alloy Y. The zirconia particles can only be found in the outer part of the alumina scale. They possess a different (equiaxed) morphology and are larger in size than at 1,200 °C. The morphological and size variations between the zirconia particles formed at 1,200 and 1,300 °C can be explained in terms of a temperature dependence of the internal oxidation process. The results are in excellent agreement with the observations of Megusar and Meier [27], who studied internal oxidation of Ti in Co–Ti alloys. These authors found that the size and the morphology of the internal precipitates are determined by the competition between the nucleation and growth of internal oxides, which is directly related to the velocity of the internal oxidation front. Fast oxygen penetration as well as high oxide stability promote nucleation of the internal oxide particles and consequently a finer precipitate size. Elongated internal oxide precipitates occur, when the rate of oxygen penetration is approximately equal to the rate of solute diffusion in the alloy, as it is apparently the case for Alloy Y + Zr at 1,200 °C. With increasing temperature, the alloy diffusion is accelerated to a larger extent than the oxygen penetration resulting in a suppressed nucleation and preferential growth of the internal oxide particles, as can be observed in Alloy Y + Zr at 1,300 °C.

The absence of zirconia particles in the inner part of the alumina scale on Alloy Y + Zr at 1,300 °C is an indication of the Zr depletion from the alloy, as described previously [26]. The Zr depletion from the alloy leads to a change of the oxide microstructure in the inner part of the scale, where a columnar grain structure is found similar to that on the Zr-free Alloys Y and Y + Ti. Consequently the "apparent" instantaneous parabolic rate $K'_p(t)$ of Alloy Y + Zr decreases with increasing the exposure time, and after 50 h at 1,300 °C its absolute value starts to be lower than that at 1,200 °C. The effect of Zr depletion on the oxidation rate has been verified in TG experiments on specimens with different thickness corresponding to different Zr reservoirs as shown in Ref. [26]. In Fig. 11, the values of "apparent" instantaneous parabolic rate constant, $K'_p(t)$ calculated from the TG data in Fig. 6 for 1 mm thick sample and those from Ref. [26] for the 0.3 mm thick sample are plotted as a function of scale thickness superimposed over the respective SEM cross-sections. It is obvious that the instantaneous scale growth rate drops as soon as the Zr incorporation into the scale diminishes due to Zr depletion in the alloy. This occurs earlier (i.e. at a smaller oxide thickness) for the thinner specimen with a smaller Zr reservoir. Figure 12 illustrates schematically the

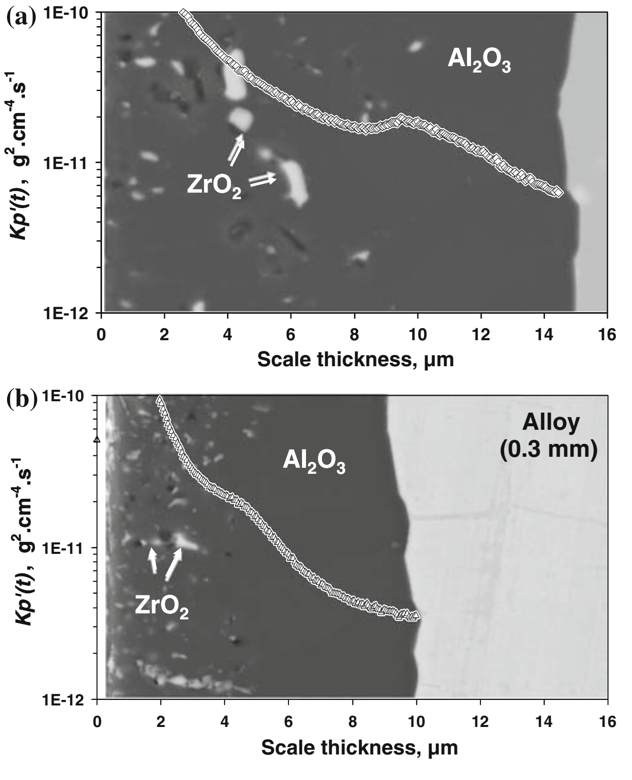

**Fig. 11** SEM cross-section of Alloy Y + Zr after 96 h isothermal oxidation at 1,300 °C in Ar–20%$O_2$ superimposed with the plot of "apparent" instantaneous parabolic rate constant derived from the mass change data in Fig. 6 for specimen thickness of 1.0 mm (**a**) and from Ref. [26] for specimen thickness 0.3 mm (**b**)

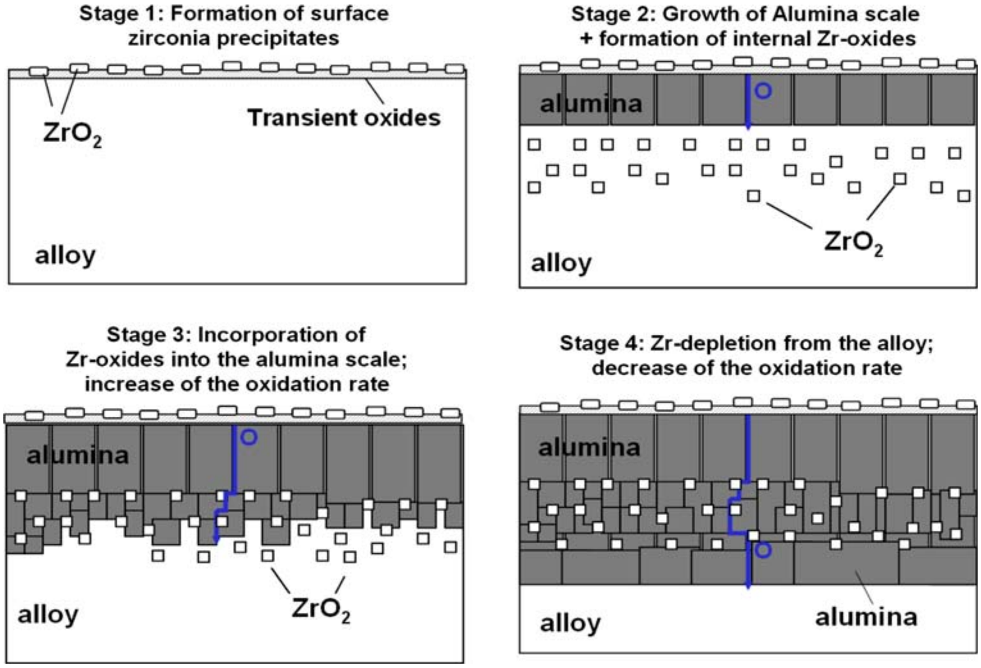

**Fig. 12** Schematic illustrating the mechanism of Zr incorporation into the alumina scale during isothermal oxidation for a specimen of finite thickness

mechanism of the Zr incorporation into the alumina scale and its depletion from the alloy matrix as well as their respective effects on the scale microstructure.

### Effect of Hf on the alumina scale microstructure and growth rate

Qualitatively similar to Alloy Y + Zr in Alloy Y + Hf, incorporation of Hf into the scale prevailed and that of Y was suppressed. At both test temperatures no Y–Al-mixed oxides were found within the scale or in the sub-scale zones of Alloy Y + Hf by EDX and XRD analyses. Rather at 1,200 °C Hf was present in the alumina scale in the form of occasional elongated hafnia and Y/Hf-mixed oxide particles, the latter being associated with the alloy grain boundaries. In contrast, at 1,300 °C the hafnia particles were found to be finer and more homogeneously distributed in the scale as well as in the sub-scale regions. This variation in the morphology and distribution of the hafnia particles with temperature is in agreement with the considerations of internal oxidation principles [27] as discussed above for Alloy Y + Zr. At 1,200 °C, the Hf diffusion in the bulk alloy is apparently slow, and thus its transport from the bulk alloy towards the sub-scale regions occurs more readily via short-circuit paths (alloy grain boundaries). This assumption explains why at 1,200 °C hafnia precipitates are found mainly at the alloy grain boundaries. In contrast at 1,300 °C the Hf diffusion in bulk is accelerated, thus allowing formation of small homogeneously distributed hafnia precipitates. An interesting observation regarding the Hf incorporation is, however, that in spite of the significant amount of the hafnia precipitates within the alumina scale at 1,300 °C no increase in the scale growth rate was observed for Alloy Y + Hf as was the case of Alloy Y + Zr. One of the possible explanations to this effect could be that the oxygen transport in hafnia is slower than that in zirconia [23]. However, the growth rate of the alumina scale on Alloy Y + Hf is even smaller than that of Alloys Y and Y + Ti, i.e. the materials forming nearly single-phase alumina scales with only minor amounts of RE oxide inclusions. Similar observations were made by other authors on reduction of the alumina scale growth rate by addition of Hf to FeCrAlY alloys [8, 10] and NiPtAl [28]. An additional effect might, therefore, be responsible for the exceptionally low growth rates of the alumina scales on Alloy Y + Hf, e.g. a more effective co-doping of the alumina grain boundaries by Y and Hf compared to the single Y doping as suggested in [8].

### The effect of IVa elements in commercial FeCrAlY alloys

The presented results with the high-purity model FeCrAlY alloys demonstrate which modifications to the scale growth mechanism and rate would be generally expected if minor amounts of group IVa elements are added to the alloy. However, this might not in all cases be directly extrapolated to commercial FeCrAl alloys. Because of higher contents of impurities, such as carbon and nitrogen in commercial FeCrAl alloys, the IVa elements could be to a large extent tied up in various carbide and/or nitride phases. On one hand, this can result in a slower incorporation of the IVa elements into the alumina scale as internal oxides. It was shown recently by Nychka and Clarke [7] that the mere presence of the REs as a single or combined addition in the alloy does not necessarily lead to effective doping of the alumina scales, which might exhibit a significant portion of outward growth as commonly observed in RE-free materials. On the other hand, if formed in the sub-surface alloy regions, the carbide and nitride precipitates can become incorporated into the scale as described recently in Ref. [9]. Upon incorporation into the scale these precipitates may be transformed into oxide phases after longer times resulting in local scale cracking and porosity formation [9] accelerating the scale growth.

Finally it should be emphasised that the observed effects of the IVa element additions on the scale microstructure and growth kinetics are related to their reservoirs rather than concentrations. In typical applications of commercial FeCrAl alloys with RE contents of typically 0.02–0.05 mass%, such as car catalyst carriers or fibre mats for clean gas burners (component thickness of 20–50 μm), the reservoirs of Zr and Hf are very small. Consequently, they are expected to be depleted quite rapidly during oxidation having only a minor effect on the scale microstructure and growth rate at longer exposure times.

## Conclusions

The effects of group IVa elements to FeCrAl, Y-containing alloys on the alumina scale formation have been studied. Due to their high oxygen affinity and mobility in the alloy matrix Zr and Hf were found to become enriched at the surface in the initial stages of oxidation, thus suppressing Y-oxide formation at the surface. At longer exposure times the incorporation of Zr and Hf into the alumina scale occurs in the form of internal oxide precipitates. The precipitate morphology and the distribution are determined by competition of their nucleation and growth, therefore being dependent on the Zr (Hf) reservoirs and mobility in the alloy as well as oxidation temperature.

Upon incorporation into the scale, the $ZrO_2$ precipitates decrease the alumina grain size and provide short-circuit diffusion paths for oxygen by themselves as well as through the associated porosity, resulting in increased alumina scale growth rate. At longer exposure times a Zr depletion from the alloy occurs, after which the microstructure of the alumina scale starts to exhibit large columnar grains, similar to those observed on the FeCrAlY-alloy without Zr.

The mechanism of Hf incorporation into the scale is similar to that of Zr; however, the Hf internal oxidation and incorporation into the scale occurred at a slower rate. This might be related to the lower Hf content in the studied material and/or to a slower Hf mobility in FeCrAl-alloy matrix than those of Zr. The incorporation of hafnia particles into the alumina scale did not result in a higher scale growth rate. Moreover, the scale growth rate on the Y and Hf co-doped alloy was even smaller than that on the Hf-free, Y-doped alloy.

Under the studied conditions only minor Ti incorporation into the alumina scale occurred and consequently no significant effect of this element on the scale microstructure was observed. It is most likely related to a lower thermodynamic stability of titanium oxides compared to that of alumina under the prevailing Ti and Al activities in the alloy, so that Ti incorporation via an internal oxidation process is not possible.

**Acknowledgements** The authors are grateful to J. Le-Coze from Ecole des Mines de Saint-Etienne for manufacturing of the high-purity model alloys and to E. Wessel from Forschungszentrum Jülich GmbH for the SEM studies. Part of the work was performed in the EU project SMILER (Project No. G5RD-CT-2001-00530). D. Naumenko would like to thank the Deutsch Forschungsgemeinschaft (DFG) for the financial support of his work.

## References

1. Whittle DP, Stringer J (1980) Philos Trans R Soc Lond A 295:309
2. Quadakkers WJ, Bennett MJ (1994) Mater Sci Technol 10:126
3. Smeggil JG, Funkenbusch AW, Bornstein NS (1986) Met Trans A 17:923
4. Hou PY, Stringer J (1992) Oxid Met 38(5/6):323
5. Quadakkers WJ, Holzbrecher H, Briefs KG et al (1989) Oxid Met 32(1/2):67
6. Pint BA (1996) Oxid Met 45(1/2):1
7. Nychka JA, Clarke DR (2005) Oxid Met 63(5/6):325
8. Pint BA (2003) J Am Ceram Soc 86(4):686
9. Quadakkers WJ, Naumenko D, Singheiser L et al (2000) Mater Corros 51:350
10. Klöwer J, Kolb-Telieps A, Brede M (1997) In: Bode H (ed) Proceedings of the international conference on metal supported automotive catalytic converters. Werkstoff-Informationsgesselschaft mbH, Frankfurt, pp 33–46
11. Ishii K, Kohno M, Ishikawa S, Satoh S (1997) Mater Trans JIM 38(9):787
12. Gray T H (1997) In: Bode H (ed) Proceedings of the international conference on metal supported automotive catalytic converters. Werkstoff-Informationsgesselschaft mbH, Frankfurt, pp 47–54
13. Kochubey V, Naumenko D, Wessel E et al (2006) Mater Let 60:1654
14. Reddy KPR, Smialek JL, Cooper AR (1982) Oxid Met 17(5/6):429
15. Basu SN, Halloran JW (1987) Oxid Met 27(3/4):143
16. Quadakkers WJ, Naumenko D, Wessel E et al (2004) Oxid Met 61(1/2):17
17. Quadakkers WJ (1990) Mater Corros 41:659
18. Liu Z, Gao W, He Y (2000) Oxid Met 53(3/4):341
19. Naumenko D, Gleeson B, Wessel E et al (2007) Metal Mater Trans 38A:2974
20. Domagala RF, Rausch JJ, Levinson DW (1961) Trans ASM 53:139

21. Arias D, Abriata JP (1988) Bull Alloy Phase Diag 95:597
22. Okamoto H (1993) In: Okamoto H (ed) Phase diagrams of binary iron alloys. ASM International, Materials Park, OH, USA, pp 12–28
23. Kofstad P (1988) High temperature corrosion. Elsevier Applied Science Publishers, Barking, UK
24. Pint BA (1997) Oxid Met 48(3/4):303
25. Mommer N, Lee T, Gardner JA (2000) J Mater Res 15(2):377
26. Wessel E, Kochubey V, Naumenko D et al (2004) Scr Mater 51(10):987
27. Megusar J, Meier GH (1976) Metal Trans 7A:1133
28. Izumi T, Mu N, Zhang L, Gleeson B (2007) Surf Coat Technol 202:628